Astron. Astrophys. 332, 1123–1132 (1998)

ASTRONOMY AND ASTROPHYSICS

Thermal physics of asteroids

IV. Thermal infrared beaming

Johan S.V. Lagerros⋆

Uppsala Astronomical Observatory, Box 515, S-751 20 Uppsala, Sweden (WWW: http://www.astro.uu.se/)

Received 17 November 1997 / Accepted 13 January 1998

Abstract. The so called beaming is an important factor when studying the thermal emission from the atmosphereless bodies of the solar system. The emission is non-Lambertian and has a tendency to be "beamed" in the solar direction. The small scale surface roughness is probably the main source of the effect.

In this paper, the problem is studied theoretically by adding roughness to Lambertian surfaces, and investigate the change in the emission. The radiative transfer problem in the visual and IR is considered and solved simultaneously with the heat conduction problem. This gives the temperature variations over the surface, as caused by shadows and varying slopes on the surface. The beaming is derived by comparing the emission from the rough and smooth surface.

Two types of roughness approaches are considered. Analytical solutions to the temperature variations are given for surfaces covered with hemispherical segment craters. Numerical methods are used for stochastic surfaces. The latter approach to the roughness is probably closer to the real surfaces, but the former is far easier to apply in practise. The qualitative results of the two surface types are the same. The beaming is enhanced by the increasing the root mean square (r.m.s.) slope, or by increasing the albedo. The beaming produced by the two approaches for a given r.m.s. slope is rather close for a 60 % crater coverage in the spherical crater case.

The combined effects of heat conduction and the surface roughness is studied. In many cases it is, however, possible to treat them separately which is of major practical importance.

As an example, IRAS data (Tedesco et al., 1992) of the asteroid 3 Juno is compared to model thermal light curves produced, with good agreement.

Key words: minor planets, asteroids – radiation mechanisms: thermal – infrared: solar system – Moon – planets and satellites: individual: 3 Juno

1. Introduction

The thermal emission from atmosphereless bodies, such as the Moon, Mercury, or the asteroids, is strongly affected by the roughness and porosity of their surfaces. On a rough surface effects due to multiple scattering, shadows, and mutual heating are important. The solar radiation can penetrate and heat the porous surface material to some depth, and in addition to conduction, heat is transfered by radiation. The lack of convective heat transfer within a dense atmosphere, and the very low thermal conductivity of the surface material, results in large temperature variations on rather small scales.

Thus the emission is not that of a smooth flat surface, but rather the weighted sum of black body radiators at different temperatures, convolved with a material dependent emissivity. As a result the observed brightness temperature of the full Moon varies with the zenith angle θ as $a + b\cos\theta$, rather than $\cos^{1/4}\theta$ expected for a Lambertian surface (Saari and Shorthill, 1972). In the Standard Thermal Model of asteroids (STM) (Lebofsky and Spencer, 1989, and references therein), the opposition brightness temperature has to be increased by the empirical beaming parameter, and the slope of the phase curves are steeper than the Lambertian phase curve. Thus the tendency is to emit or "beam" more in the solar direction at the expense of the emission at larger phase angles.

Many authors have worked on various theoretical models to describe the beaming effects. Most popular are perhaps models where the surface roughness is described by spherical (Buhl et al., 1968; Winter and Krupp, 1971; Hansen, 1977; Spencer, 1990) or parabolic "craters" (Vogler et al., 1991; Johnson et al., 1993). Jämsä et al. (1993) used a stochastic surface, described by a Gaussian correlation function. The radiative transfer in the regolith has been studied by e.g. Henderson and Jakosky (1994) and Hapke (1993; 1996b). Hapke (1996a) came to the conclusion that only about 20 % of the observed beaming phenomena can be explained by effects in the porous media.

As has been pointed out by Johnson et al. (1993) there is a risk of confusing surface roughness effects and trends in the emissivity. As the beaming offers the opportunity to directly investigate the surface texture of the asteroids, it also makes the compositional studies in the thermal IR more complicated. Furthermore, as discussed in Paper I (Lagerros, 1996a), the beaming correlates with the global shape of the non-spherical asteroids. For that reason, both disk-integrated data (asteroids most of which are likely to have irregular shapes) and disk-resolved data (e.g. the Moon or Mercury) are potentially in need of detailed beaming models.

⋆ e-mail: Johan.Lagerros@astro.uu.se

A thermophysical model of asteroids have been outlined in Papers I–III (Lagerros 1996a; 1996b; 1997). Heat conduction into the regolith, surface roughness, microwave emission, and irregular shapes have been considered. In this paper the beaming effects are followed up in more detail. The radiative transfer problem for the rough surface is formulated as a set of integral equations. Analytical solutions are derived for the roughness model using spherical craters. This makes the model easy to implement, but it is based on a highly idealised geometry. To investigate the limitations of this approach, a numerical method is applied to a stochastic surface. As a concluding example the thermophysical model is applied to IRAS data of 3 Juno.

2. Beaming physics

The thermal models outlined in the Papers I–III divides the surface of the asteroid into typically a few thousand planar facets. The facets are heated by the Sun and scattered visual and thermal radiation from neighbouring facets. As the asteroid rotates, much of the heat is absorbed during the daytime and is later re-emitted on the night side, due to the heat conduction into the material below the surface of the facets. The predicted flux at a given wavelength λ and distance D from the asteroid, is computed by integrating the contribution from each facet, such that

$$F_\lambda = \frac{1}{D^2} \oint I_\lambda(S) \mu \, dS, \tag{1}$$

where I_λ is the intensity from a point S on the surface, in the direction towards the observer, and μ the directional cosine of the facet dS. If dS is out of sight, $\mu = 0$ by definition. The intensity I_λ is essentially the Planck function, multiplied by the wavelength and directional dependent emissivity.

The problem with this, however, is that there will be substantial temperature variations even on small scales due to the rough terrain. The emission from a facet is not that of a *single* black body radiator at a given temperature.

Here the assumption is that the beaming effects are caused by the surface roughness on a very small scale, but still large enough for the geometric optics approximation to be valid. On a scale too small, the temperature variations will be smeared by the heat conduction. Therefore the methods outlined in Paper III can be applied here, but now on a much smaller scale.

Roughness is added to a small part of the planar facet. The coordinate system used is to let the xy-plane coincide with the facet, and have the z-axis pointing outwards from the surface. The rough surface is described by $z = z(x, y)$. The emission from this rough patch is then compared to that of a flat surface with the same projected area, which gives a correction factor for the whole facet.

Both approaches to the surface roughness discussed here are isotropic, i.e. no preferred azimuth direction. In the first case are craters shaped as hemispherical segments covering a given fraction of the flat surface. The second is a Gaussian random surface, completely described by the r.m.s. slope ρ.

As in Paper III, the spectrum is divided into the visual (V) where the solar irradiation dominates, and the infrared (IR) where the thermal emission takes place. The temperature variations over the rough surface is determined by solving the multiple scattering problem in the V and IR bands. Both internal and external shadows have to be considered. The heat conduction into the regolith is taken into account, but only in one dimension. The observed flux in different directions is compared to the flux from a smooth surface with the same physical properties.

Table 1. The notation.

$\alpha_{\rm V}$	V absorptivity
$c_{\rm s}$	regolith heat capacity
c_0	speed of light
D	distance to the observer
$\varepsilon_{\rm IR}$	IR emissivity
h	Planck's constant
$J_{\rm V}$, $J_{\rm IR}$	V and IR radisoity
k	Boltzmann's constant
$\kappa_{\rm s}$	regolith thermal conductivity
λ	wavelength
m_0, m	local solar and observer directional cosines
μ_0, μ	directional cosines of the mean surface
R	distance to the Sun (in AU)
ω	angular rotational velocity of the body
$\rho_{\rm s}$	regolith density
$S_\odot$	solar constant
σ	Stefan-Boltzmann constant

2.1. Notation

The notation used here is given in Table 1. Since it is preferable to work in normalised units:

$\mathcal{J}$	$= J/(S_\odot/R^2)$	normalised radiosity
$T_{\rm SS}^4$	$= \alpha_{\rm V} S_\odot/\varepsilon_{\rm IR}\sigma R^2$	Sub-solar temperature
u	$= T/T_{\rm SS}$	normalised temperature
Θ	$= \sqrt{\kappa_{\rm s}\rho_{\rm s}c_{\rm s}}\sqrt{\omega} \;/\; \varepsilon_{\rm IR}\sigma T_{\rm SS}^3$	thermal parameter
X	$= hc_0/\lambda k T_{\rm SS}$	
t'	$= \omega t$	normalised time

With this the Planck function becomes

$$B_\lambda = \frac{2\pi h c_0^2}{\lambda^5} \cdot \frac{1}{\exp(X/u) - 1} \tag{2}$$

2.2. Radiative transfer

View factors have been used several times before in order to solve the radiative heat transfer problem on rough surfaces in the solar system (Hansen, 1977; Spencer, 1990; Vogler et al., 1991; Johnson et al., 1993; Lagerros, 1996a). A more general introduction is given by Modest (1993). The view factor from a facet da at a point $\boldsymbol{r}$ to da' at $\boldsymbol{r}'$ is defined as the fraction of the radiative energy leaving the first and directly striking the latter. Assuming Lambertian facets, the view factor is

$$\begin{aligned} dF_{da\to da'} &= \mathcal{F}(\boldsymbol{r},\boldsymbol{r}')\, da' \\ &= v(\boldsymbol{r},\boldsymbol{r}') \frac{\big(\hat{\boldsymbol{n}}\cdot(\boldsymbol{r}'-\boldsymbol{r})\big)\big(\hat{\boldsymbol{n}}'\cdot(\boldsymbol{r}-\boldsymbol{r}')\big)}{\pi|\boldsymbol{r}-\boldsymbol{r}'|^4}\, da' \end{aligned} \tag{3}$$

where $\hat{\boldsymbol{n}}$ and $\hat{\boldsymbol{n}}'$ are the corresponding surface normals, and $v(\boldsymbol{r},\boldsymbol{r}')$ is 1 if the two facets are visibile to each other, otherwise it is taken to be 0.

The radiosity $\mathcal{J}_{\rm V}(\boldsymbol{r})$ is the total flux of visual light reflected from a point $\boldsymbol{r}$. This is given by multiplying the total irradiation at $\boldsymbol{r}$ by the reflectance $1-\alpha_{\rm V}(\boldsymbol{r})$. Since the irradiation equals the insolation plus the radiosity from other parts of the surface, it follows that

$$\frac{\mathcal{J}_{\rm V}(\boldsymbol{r})}{1-\alpha_{\rm V}(\boldsymbol{r})} - \int_A \mathcal{J}_{\rm V}(\boldsymbol{r}')\mathcal{F}(\boldsymbol{r},\boldsymbol{r}')\,da' = m_0(\boldsymbol{r}) \tag{4}$$

For the IR the source term of the thermal emission is $u^4(\boldsymbol{r})$, by which

$$\frac{\mathcal{J}_{\rm IR}(\boldsymbol{r})}{1-\varepsilon_{\rm IR}(\boldsymbol{r})} - \int_A \mathcal{J}_{\rm IR}(\boldsymbol{r}')\mathcal{F}(\boldsymbol{r},\boldsymbol{r}')\,da' = \frac{\alpha_{\rm V}(\boldsymbol{r})u^4(\boldsymbol{r})}{1-\varepsilon_{\rm IR}(\boldsymbol{r})} \tag{5}$$

The temperature u is determined by the energy balance between the energy thermally emitted, the heat conducted into the regolith, the radiation from the neighbouring facets and the Sun, such that

$$\begin{aligned} u^4(\boldsymbol{r}) = {} & -\Theta(\boldsymbol{r})\hat{\boldsymbol{n}}\cdot\nabla u(\boldsymbol{r}) + m_0(\boldsymbol{r}) \\ & + \int_A \left(\mathcal{J}_{\rm V}(\boldsymbol{r}') + \frac{\varepsilon_{\rm IR}(\boldsymbol{r})}{\alpha_{\rm V}(\boldsymbol{r})}\mathcal{J}_{\rm IR}(\boldsymbol{r}')\right)\mathcal{F}(\boldsymbol{r},\boldsymbol{r}')\,da' \end{aligned} \tag{6}$$

where the gradient ∇ is for Cartesian coordinates normalised by the thermal skin depth $l_{\rm s} = \sqrt{\kappa_{\rm s}/\rho_{\rm s}c_{\rm s}\omega}$. Note the dependency on the thermal history – as the asteroid rotates – of u in Eqs. (5) and (6), if $\Theta > 0$. On the other hand, if heat conduction can be neglected due to the slow spin rate of the body, or the low conductivity of the regolith, the thermal parameter is $\Theta(\boldsymbol{r}) = 0$. By combining Eq. (5) and Eq. (6) it follows that

$$\mathcal{J}_{\rm IR}(\boldsymbol{r}) - \int_A \mathcal{J}_{\rm IR}(\boldsymbol{r}')\mathcal{F}(\boldsymbol{r},\boldsymbol{r}')\,da' = \frac{\alpha_{\rm V}(\boldsymbol{r})}{1-\alpha_{\rm V}(\boldsymbol{r})}\mathcal{J}_{\rm V} \tag{7}$$

These Fredholm integral equations of the second kind have to be solved starting with $\mathcal{J}_{\rm V}$ in Eq. (4). If there is no heat conduction, $\mathcal{J}_{\rm IR}$ is given by Eq. (7). Otherwise, the IR radiosity has to be derived by iterating between Eq. (6) and Eq. (5), as described in Paper III. Only in a few special cases is it possible to find analytical solutions. In general the rough surface has to be divided into a finite number of facets. By this the kernel $\mathcal{F}$ is replaced by the view factor matrix F, and the integral equations are turned into matrix equations. A high precision method for calculating the view factor between finite triangular facets is given in Sect A.1.

The final step is to compute the integrated flux from the surface towards the observer:

$$\begin{aligned} F_\lambda = {} & \frac{1}{\pi D^2}\int_A\int_A da\,da'\,m(\boldsymbol{r})\varepsilon_{\rm IR}(\boldsymbol{r}')B_\lambda(T(\boldsymbol{r}')) \\ & \left[\delta(\boldsymbol{r}-\boldsymbol{r}') + \big(1-\varepsilon_{\rm IR}(\boldsymbol{r})\big)\mathcal{F}(\boldsymbol{r},\boldsymbol{r}')\right] \end{aligned} \tag{8}$$

The model described here allows for inhomogeneous surface material since both the absorptivity and emissivity may vary over the surface (e.g mineral mixtures). This possibility is not explored any further. The $\alpha_{\rm V}$ and $\varepsilon_{\rm IR}$ are taken to be constant over the surface, which also results in constant sub-solar temperature $T_{\rm SS}$, and thermal parameter Θ.

2.3. Spherical craters

As discussed above, spherical "craters" on a smooth surface have been used several times as a surface roughness model. Typically the hemispherical segments cover a fraction f of the surface. The shape of the craters is described by S, the depth of the segment divided by the diameter of the sphere. Without loss of generality, the radius of the sphere can be taken to be unity. The surface area of the segment is then $A = 4\pi S$, and the area of the reference surface or the projected area of the crater rim is $A_{\rm ref} = 4\pi S(1-S)$.

Due to the symmetries of the sphere it is possible to solve the integral equations analytically. Buhl et al. (1968) made use of this, but assumed the emissivity to equal 1, and neglected the scattered visual radiation. The approach here is more general.

The view factors inside a sphere (Modest, 1993) are given by

$$dF_{da\to da'} = \mathcal{F}(\boldsymbol{r},\boldsymbol{r}')\,da' = \mathcal{F}(\boldsymbol{r}')\,da' = \frac{d\Omega'}{4\pi} \tag{9}$$

if $d\Omega' = \sin\theta'\,d\theta'\,d\phi'$ in spherical coordinates, with $\theta' = 0$ at the bottom of the crater. This means that the kernel $\mathcal{F}(\boldsymbol{r},\boldsymbol{r}')$ in the integral equations above is independent of $\boldsymbol{r}$, and thus also the integrals.

Thus Eqs. (4), (5) and (6) can be written in respective order:

$$\frac{\mathcal{J}_{\rm V}(\theta,\phi)}{1-\alpha_{\rm V}} - K_1 = m_0(\theta,\phi) \tag{10}$$

$$\frac{\mathcal{J}_{\rm IR}(\theta,\phi)}{1-\varepsilon_{\rm IR}} - K_2 = \frac{\alpha_{\rm V}}{1-\varepsilon_{\rm IR}}u^4(\theta,\phi) \tag{11}$$

$$u^4(\theta,\phi) = -\Theta\hat{\boldsymbol{n}}\cdot\nabla u(\theta,\phi) + m_0(\theta,\phi) + K_3 \tag{12}$$

where K_1, K_2 and K_3 are constants. Again, if heat conduction can be neglected, Eq. (7) can be used, and is transformed into

$$\mathcal{J}_{\rm IR}(\theta,\phi) - K_4 = \frac{\alpha_{\rm V}}{1-\alpha_{\rm V}}\mathcal{J}_{\rm V}(\theta,\phi) \tag{13}$$

where K_4 is a constant. All these constant can easily be found by using the same procedure. For example, solving Eq. (10) for $\mathcal{J}_{\rm V}(\boldsymbol{r})$ and substituting it into the definition of the constant K_1 gives

$$K_1 = \int_A \mathcal{J}_{\rm V}(\boldsymbol{r}')\mathcal{F}\,da' = \int_A (1-\alpha_{\rm V})\big(K_1 + m_0(\theta',\phi')\big)\,\frac{d\Omega'}{4\pi}$$

It is useful to note that

$$\int_A \frac{d\Omega'}{4\pi} = S \qquad \text{and} \qquad \int_A m_0(\theta',\phi')\frac{d\Omega'}{4\pi} = S(1-S)\mu_0$$

where the latter expression comes from the fact that the total energy entering the crater has to pass the projected area of the crater rim. From this it follows that

$$K_1 = \frac{1-\alpha_{\rm V}}{1-S(1-\alpha_{\rm V})}S(1-S)\mu_0 \tag{14}$$

$$K_2 = \frac{\alpha_{\rm V}}{1-(1-\varepsilon_{\rm IR})S}\int_A u^4(\theta',\phi')\frac{d\Omega'}{4\pi} \tag{15}$$

$$K_3 = K_1 + \frac{\varepsilon_{\rm IR}}{\alpha_{\rm V}}K_2 \tag{16}$$

Thus the radiosity $\mathcal{J}_{\rm v}$ equals the local directional cosine m_0 plus a constant radiation field, regardless of the position in the hemispherical segment "crater". Again, a solution can be found by first calculating K_1 and then iterating between Eqs. (11) and (12).

With no heat conduction

$$K_4 = \frac{\alpha_{\rm v}}{1 - S(1-\alpha_{\rm v})} S\mu_0 \tag{17}$$

and from Eq. (13),

$$\begin{aligned} u^4(\theta,\phi) &= m_0(\theta,\phi) + K_1 + \frac{\varepsilon_{\rm IR}}{\alpha_{\rm v}} K_4 \\ &= m_0(\theta,\phi) + \frac{(1-S)(1-\alpha_{\rm v}) + \varepsilon_{\rm IR}}{1 - S(1-\alpha_{\rm v})} S\mu_0 \end{aligned} \tag{18}$$

That is, the temperature is determined by the direct solar irradiation and a constant term, which is the same for the whole crater.

If z_0 is the zenith distance ($\mu_0 = \cos z_0$) and ϕ_0 is the azimuth of the Sun, the local directional cosine is given by first calculating

$$\widetilde{m}_0(\theta,\phi) = \cos z_0 \cos\theta - \sin z_0 \sin\theta \cos(\phi - \phi_0)$$

and then taking care of the shadow from the crater rim

$$m_0(\theta,\phi) = \begin{cases} \widetilde{m}_0(\theta,\phi) & \text{if} \quad 2\,\widetilde{m}_0 \cos z_0 > \cos\theta + 2S - 1 \\ 0 & \text{otherwise} \end{cases}$$

The same method of course applies to $m(\theta,\phi)$.

The final step is to compute the observed flux from Eq. (8)

$$\begin{aligned} F_\lambda = \frac{\varepsilon_{\rm IR}}{\pi D^2} \Bigg(& \int_A m(\theta,\phi) B_\lambda\big(u(\theta,\phi)\big)\, d\Omega \\ & + (1-\varepsilon_{\rm IR}) S(1-S)\mu \int_A B_\lambda\big(u(\theta,\phi)\big)\, d\Omega \Bigg) \end{aligned} \tag{19}$$

This flux should then be compared to the flux from the reference surface

$$F_{\lambda,\rm ref} = \frac{\varepsilon_{\rm IR}}{\pi D^2} B_\lambda(u_{\rm ref}) \mu A_{\rm ref}$$

where $u_{\rm ref} = \mu_0^{1/4}$ if heat conduction is neglected.

The procedure is then basically to calculate u from for example Eq. (18) and then numerically integrate the flux from Eq. (19). If the crater coverage is a fraction f, the flux to be compared with the reference flux $F_{\lambda,\rm ref}$ is simply $fF_\lambda + (1-f)F_{\lambda,\rm ref}$.

An important issue is correcting the albedo for the surface roughness. For a spherical asteroid, the Bond albedo equals the bi-hemispherical reflectance. That is, the fraction of incoming light scattered in all directions from the surface, if isotropically illuminated. For the spherical crater this isotropic field $\mathcal{J}_{\rm v,ref}$ is passing through the crater rim. From Eq. (9) and basic view factor algebra, the source term m_0 in Eq. (10) is replaced by $(1-S)\mathcal{J}_{\rm v,ref}$. Using view factor algebra, the local radiosity $\mathcal{J}_{\rm v}$ adds up to the flux $\mathcal{G}_{\rm v,ref}$ passing out from the rim. From this the bi-hemispherical albedo of the spherical crater is

$$\frac{\mathcal{G}_{\rm v,ref}}{\mathcal{J}_{\rm v,ref}} = \frac{(1-\alpha_{\rm v})(1-S)}{1 - S(1-\alpha_{\rm v})}$$

Taking the crater coverage f into account, the bi-hemispherical reflectance becomes

$$r_{\rm hh} = f\frac{(1-\alpha_{\rm v})(1-S)}{1 - S(1-\alpha_{\rm v})} + (1-f)(1-\alpha_{\rm v}) \tag{20}$$

since geometric optics is assumed.

The roughness of the Gaussian random surfaces to be discussed next is measured by ρ, the r.m.s. of the slopes on the surface. For the hemispherical segment model, the corresponding value is

$$\rho^2 = f\frac{\ln(1-2S) - 2S(S-1)}{4S(S-1)}$$

which will be used when comparing the models. Note that this measure of the roughness fails when the segments becomes hemispheres, since $\rho \to \infty$ when $S \to 1/2$.

2.4. Gaussian random surfaces

A real rough surface is the result of a number of stochastic processes, rather than perfect craters forming on a flat surface. A more realistic model is probably to assume some random distribution of surface slopes or heights relative to a mean reference surface. A method to generate stochastic surfaces is discussed in Sect. A.2.

The Gaussian random surfaces in Sect. A.2. are controlled by only one parameter, the r.m.s. slope ρ. The algorithm gives the height $z = z(x,y)$ above the mean plane in a square grid. Each side in the grid has a length $2L$ and consists of $2(N+1)$ points. As illustrated in Fig. 1 the surfaces are triangulated by simply dividing each square of neighbouring points in the mesh into two triangles. The result is a rough surface described by a discrete set of facets, with well defined surface areas and normals.

All points within the spherical crater are visible to each other. The only shadows to consider are the "external", those created by the crater rim when viewed or illuminated from an external point. For the stochastic surfaces the visibility of a given point to other points on the surface or positions outside the surface is more complex. A given point is obviously not visible if its surface normal is oriented away from the other position in question. If the two facets are facing each other, it is necessary to check for other triangles obstructing the connecting line. This was achieved by using standard ray tracing methods from the computer literature (Glassner, 1990, Chap. 7).

Furthermore, to avoid unwanted effects close to the boundary of the square patch, the periodic nature of the Gaussian rough surface is used. All calculations involving shadows and radiative transfer are done by first shifting the facet under consideration to the centre position of the square patch. This is essentially achieved by performing the vector subtraction modulus $2L$, for points on the surface. An alternative approach would perhaps be to use only some inner region, cutting away the boundary, but that is very inefficient since the computational costs increases rapidly with N.

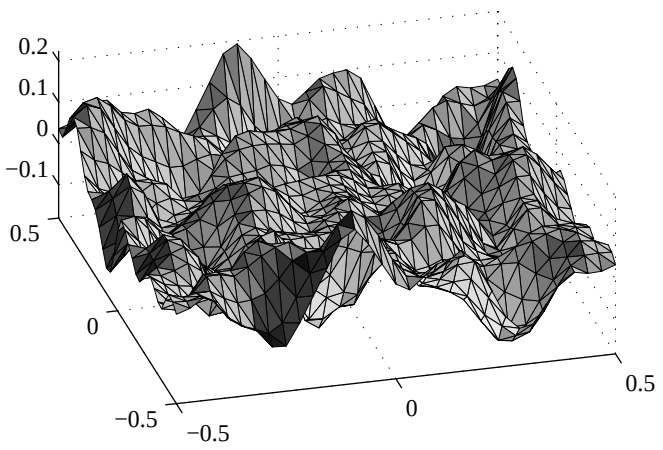

Fig. 1. A sample Gaussian random surface with r.m.s. slope $\rho = 1$, described by 2 048 triangles. The solar radiation comes from a zenith angle of 45°. Multiple scattering in the visual and the IR is taken into account, and the surface temperature is indicated by the gray scale from black (cold) to white (hot).

2.5. The constant background approximation

The integral equations in Sect. 2.2 are difficult to solve in the general case. The solutions for the spherical craters suggests a possible zeroth order approximation: the radiosity is determined by the direct solar irradiation plus a constant diffuse field (Eq. 10). This field can be derived by using the concept of self heating, as introduced in Paper III.

Assume a constant radiosity over a rough surface. The fraction of the total energy emitted escaping into space is given by the ratio $A_{\rm ref}/A$. The self heating is the fraction not escaping, but heating other parts of the surface:

$$\chi = 1 - A_{\rm ref}/A$$

From Sect. A.2 in Paper III the self heating of the surface with spherical craters is

$$\chi = \frac{Sf}{1 + S(f-1)}$$

For a Gaussian random surface, the ratio between the ensemble surface area and its projected area on the xy-plane is given by

$$1 - \chi = \sqrt{2}\rho\,\widetilde{\Gamma}(3/2, 1/2\rho^2)\,e^{1/2\rho^2} \approx 1 + \rho^2 - \rho^4 + 3\rho^6$$

where $\widetilde{\Gamma}$ is the incomplete gamma function (Muinonen and Saarinen, 1997).

The constant background field approximation is then to assume that $K_1 = \chi\langle\mathcal{J}_{\rm v}\rangle_A$. Taking the mean over the surface A in Eq. (10) results in

$$\langle\mathcal{J}_{\rm v}\rangle_A = \frac{1-\alpha_{\rm v}}{1-\chi(1-\alpha_{\rm v})}(1-\chi)\mu_0 \tag{21}$$

For the spherical craters with $f = 1$, this exactly reproduces the result in Eq. (14). This directly suggests a first comparison between the two roughness models, by numerically computing the mean and variance of $\mathcal{J}_{\rm v}/(1-\alpha_{\rm v}) - m_0$ for a sample stochastic surface.

2.6. Heat conduction

The possibility of heat conduction into the regolith is formally introduced in Eq. (6). If the thermal parameter Θ is non-zero, the heat diffusion equation has to be added to the set of equations in Sect. 2.2, that is for the interior

$$\frac{\partial u}{\partial t'} = \nabla^2 u \tag{22}$$

Strictly speaking this is a 3-D problem that has to be solved together with the integral equations for the radiative heat transfer. There are, however, limits to the length scale where the surface roughness is causing the beaming effect. The upper limit comes from the simple fact that the roughness itself must start to decrease with increasing length scales at some point. The lower limit is determined by the smearing of the lateral temperature variations due to the heat conduction. This should occur on a scale comparable to the thermal skin depth, which typically is rather small (Spencer, 1990). Within these limits, it is assumed that the conduction of heat into the regolith is more important than across the surface.

The method for solving the 1-D heat conduction problem simultaneously with the radiative heat transfer equations is discussed in Paper III. For every point on the surface the heat diffusion equation into the regolith is solved along an axis parallel to the local normal $\hat{\boldsymbol{n}}$.

2.7. The beaming function

There are several different ways to quantify the beaming. In Paper I and III a factor Λ was multiplied to the Planck function. Saari et al. (1972) corrected the brightness temperature by a "directional factor" D. Whichever approach, the correction is in principle a function of the viewing geometry, diurnal thermal history, and wavelength. The STM beaming correction, on the other hand, is primarily designed for disk integrated data of spherical asteroids. Thus the surface temperature is corrected by a factor $\eta^{-1/4}$ regardless of the position on the surface, and a linear phase correction is applied to the disk integrated flux.

The directional factors are used here, with the slight difference that the emissivity is not unity when computing the brightness temperature. The emissivity corrected brightness temperature equals the physical temperature of the surface if there is no beaming. The advantage of this approach is that the beaming correction is fairly insensitive to the effects of the heat conduction (see below). That is, if $T(\Theta)$ is the brightness temperature of a flat surface with heat conduction ($\Theta > 0$), and $T(0)$ without, then

$$\frac{\widetilde{T}(\Theta)}{T(\Theta)} \approx \frac{\widetilde{T}(0)}{T(0)} \tag{23}$$

where $\widetilde{T}$ is the brightness temperature for the same surfaces with roughness added. The temperature $T(\Theta)$ is given by the model in Paper I. If the approximation in Eq. (23) is valid, the beaming corrected $\widetilde{T}(\Theta)$ can be derived from $\widetilde{T}(0)/T(0)$. This is more desirable since introducing heat conduction as described above requires much more computational efforts.

3. Results

3.1. Implementation

A set of stochastic surfaces were generated, with the same dimensions and number of facets as in Fig. 1. Finite view factors for the triangulated surfaces were calculated by using the method described in Sect. A.1. Discrete versions (as discussed in Paper III) of the integral equations in Sect. 2.2 were employed for the stochastic surfaces. The resulting matrix equations were solved by iterative methods. The matrices involved are large ($2\,048 \times 2\,048$), but sparse and rather diagonal dominant. Therefore it is possible to find solutions in a few tens of a second on a normal workstation. The ray tracing procedures to find shadows are, however, rather costly.

The spherical craters were implemented according to the equations derived above. Heat conduction was taken into account according to Sect. 2.6. Thermal light curves were produced by using the model described in Papers I and III, and with the beaming function computed for the two types of surface roughness discussed here.

3.2. Comparing the two types of rough surfaces

The constant background approximation discussed in Sect. 2.5 is both of theoretical and practical interest. If it is valid to some degree it could be a starting point to a more advanced and realistic model than the spherical craters. On the other hand it can also be used for comparing the two roughness approaches. This is because it is exact for the hemispherical segments, with 100 % crater coverage.

The approximation was applied to stochastic surfaces with r.m.s. slopes in the range $\rho = 0.1$–1.0. The solar zenith angle was varied from 0° to 80°, and the absorptivity was assumed to be $\alpha_{\rm v} = 0.9$. Eq. (4) was solved to get the V radiosity $\mathcal{J}_{\rm v}$. For zenith angles smaller than $\sim 65^\circ$ the mean of $\mathcal{J}_{\rm v}$ is systematically lower than the value expected from Eq. (21). The difference increase with larger r.m.s. slope, but stays within 10 %.

The situation is, however, much worse for the background field. According to the approximation the radiation field from scattered light should be independent of the location, that is the quantity

$$K_1' = \mathcal{J}_{\rm v}/(1-\alpha_{\rm v}) - m_0$$

should be a constant over the surface. Relative to its mean the standard deviation of K_1' is at least 60 %. For large r.m.s. slopes and solar zenith angles the standard deviation is more than 120 %.

The conclusion is that the hemispherical segments are more efficient in "collecting" the solar radiation. In the spheres, all surface elements are participating in the scattering process. For the random surface there are valleys which to some extent behave as the spheres, but also hills with small energy exchange with the rest of the surface.

3.3. The STM beaming parameters

The STM is using an empirical correction $\eta^{-1/4}$ to the brightness temperature at opposition. Lebofsky et al. (1986) derived $\eta = 0.756$ from observations of 1 Ceres and 2 Pallas. This value has often been considered a standard value for main belt asteroids, and was used in for example the IRAS Minor Planet Survey (Tedesco et al., 1992). The open questions are how representative this value is for objects other than large main belt asteroids, and what is the physical explanation behind this and other values of η? A surface roughness model as the one presented here can be used for investigating these questions.

Model fluxes were calculated for a set of spherical non-rotating asteroids at opposition. The STM beaming parameter η was derived by fitting STM fluxes to the model fluxes, as shown in Figs. 2 and 3. The comparison with STM was made using both random surfaces, and surfaces with a 60 % coverage of hemispherical segments. With this crater coverage the two surface types produce beaming parameters $\eta = \eta(X, \rho)$ which are in rather good agreement. In the wavelength range considered here the derived beaming parameter is essentially constant. Comparing the two figures gives that increasing the albedo and the multiple scattering in the visual by lowering $\alpha_{\rm v}$ increases the beaming correction $\eta^{-1/4}$ for a given roughness ρ.

In Fig. 3, for the low albedo surfaces a rather high surface roughness is required in order to achieve $\eta = 0.756$. The $\rho \sim 0.6$ in Fig. 2 is probably more realistic, but might still be considered a bit too high. For example Jämsä et al. (1993) derived $\rho = 0.4$ for the Moon, when using the thermal emission data by Saari & Shorthill (1972).

It is very important, however, to remember that the η values derived here only includes the beaming. STM beaming parameters η obtained from observations depends not only on the beaming, but also on the wavelength, the shape, the heat conduction, the spin vector orientation, etc.

3.4. Example model of 3 Juno

The asteroid Juno was chosen as an example, since it is a rather well studied object. From visual light curves it has been possible to determine its spin vector and shape, as seen in Table 2. The table also gives the zero point of the light curve, by specifying the rotational phase for an epoch (see Sect. A.3.). The Bond albedo was computed from the geometrical albedo and the slope parameter. The surface roughness was varied, and the absorptivity $\alpha_{\rm v}$ was derived by assuming that the hemispherical albedo equals the Bond albedo in Eq. (20). The longest axis of the ellipsoid was equalled to the longest stellar occultation limb profile diameter derived by Millis et al. (1981). The emissivity was assumed to equal 0.9, and the thermal inertia taken to be close to the lunar value (Spencer, 1990).

In Fig. 4, the model is compared with IRAS data. The fluxes and error estimates were taken from the IRAS Minor Planet Survey catalogue 108 (Tedesco et al., 1992). Filter colour corrected were required (Müller, 1997). Note that the zero points of the light curves are given from the shape and spin vector solutions,

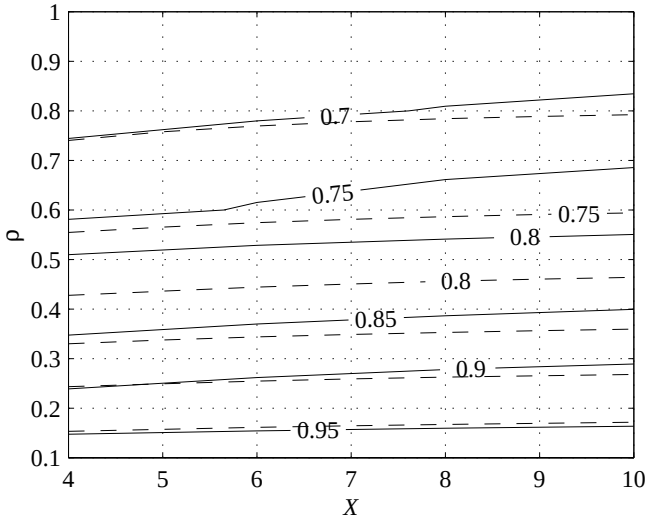

Fig. 2. The STM beaming parameter η fitted to model fluxes from spherical non-rotating asteroids, observed at opposition. The solid lines are for stochastic surfaces, and the dashed for surfaces with a 60 % coverage of hemispherical segment craters. Calculated for $\alpha_{\rm V} = 0.5$ and $\varepsilon_{\rm IR} = 0.9$.

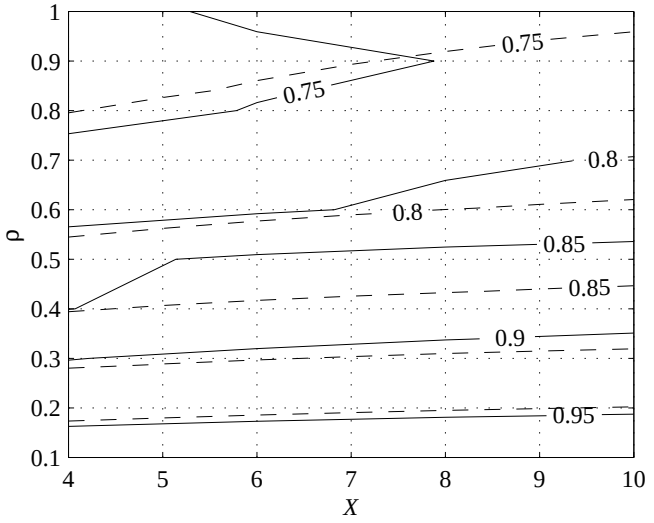

Fig. 3. Same as Fig. 2 but using $\alpha_{\rm V} = \varepsilon_{\rm IR} = 0.9$ instead.

and are not fitted to the IRAS data. The STM flux is also given, using a beaming parameter $\eta = 0.756$ and a phase correction of $0.01\,\mathrm{mag}/^\circ$.

The heat conduction was taken into account by using the detailed methods described in Sect. 2.6. The approximation discussed in Sect. 2.7 and Eq. (23) were applied as well. The agreement was found to be within 1 %, for these specific circumstances. The approximation increasingly overestimates the fluxes, with larger r.m.s. slopes, and higher thermal parameters.

4. Discussion

The beaming problem has been studied under the assumption that the small scale surface roughness is the most important factor behind the effect. The radiative heat transfer problem was formulated as a set of integral equations, which have to be solved simultaneously to give the temperature variations over the rough surface. These equations were solved for two types of surface roughness approaches. Analytical solutions were presented for a surface covered by hemispherical segment craters. A more general numerical method was devised for the stochastic surface geometries. The beaming effect was quantified by integrating the flux from the rough surfaces and compare to the flux of a similar but flat surface.

The advantage with the hemispherical segment approach is of course the analytical solutions, which makes it easy to implement. The problem is the rather idealised geometry assumed. The stochastic surfaces are in that respect probably more realistic, but much more demanding on the implementation and the computational efforts. For that reason is the comparison be-

Table 2. Physical parameters for 3 Juno.

Parameter	Value
Spin vector[a]	$\lambda_{\rm p} = 108^\circ$, $\beta_{\rm p} = +36^\circ$
Shape[1]	$a/b = 1.21$, $b/c = 1.20$
Rotational period[1]	$P_{\rm sid} = 0\overset{\rm d}{.}3003970$
Orientation[1]	$\gamma_0 = 5^\circ$ at $JD_0 = 2\,440\,587.5$
Diameter[b]	$2a = 290\,\mathrm{km}$
Geometric albedo[2]	$p_{\rm V} = 0.164$
Slope parameter[c]	$G = 0.17$
Assumed:	
Thermal inertia	$\Gamma = \sqrt{\kappa_{\rm s}\rho_{\rm s}c_{\rm s}} = 50\,\mathrm{J\,m^{-2}\,s^{-0.5}\,K^{-1}}$
Emissivity	$\varepsilon_{\rm IR} = 0.9$

[a] Per Magnusson, private communication
[b] Millis et al. (1981)
[c] Lagerkvist et al. (1992)

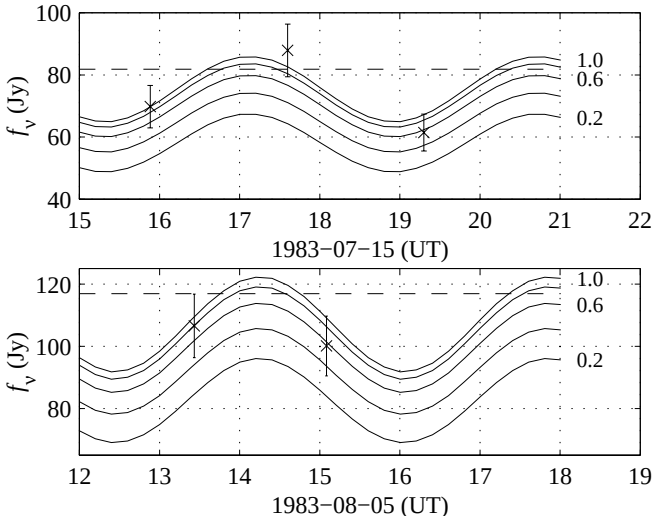

Fig. 4. IRAS data at $\lambda = 12\,\mu$m of 3 Juno, compared to model thermal light curves. Curves computed for $f = 0.8$, and r.m.s. slopes $\rho = 0.2, 0.4, \ldots, 1.0$, as indicated to the right. The dashed lines are the corresponding STM fluxes.

tween these to approaches of some interest. Since the results from the two approaches are quite similar, it is likely that the spherical crater model would be the choice in most practical applications.

The beaming, as caused by the surface roughness, can probably be understood as the result of two different effects. A smooth surface dilutes the energy received according to the well known cosine factor. The rough surface will on the other hand have facets oriented towards the Sun, which will become significantly hotter than the flat comparison surface. At opposition the observer will see the hottest facets in the most favourable geometry. This is further enhanced by the second effect, the multiple scattering. A higher albedo increases the scattered radiation, which means that parts of the surface in shadow or somewhat oriented away from the Sun also gets heated. The consequences are seen in Figs. 2 and 3 where both a larger surface roughness, and higher albedo increases the beaming.

The approximation discussed in Sect. 2.7 and Eq. (23) is an attempt to separate the beaming from the heat conduction. By this it is possible to substantially reduce the computational efforts. The agreement in the final fluxes were found to be very good between the detailed calculations and the use of the approximation for 3 Juno in Sect. 3.4. Spencer (1990) expressed this in a somewhat different way by concluding that surface roughness adds a term to the STM beaming parameter, which is independent of the heat conduction. The approximation is probably valid in most cases, which is a major practical advantage. One should, however, keep in mind that there can be problems in situations with disc resolved data, and large thermal parameters combined with very rough surfaces.

On the theoretical side do the integral equations and their analytical solutions open possibilities for future development. The constant background approach is probably bad approximation for more general surface than the hemispherical segments. The results in Figs. 2 and 3 suggests on the other hand an approach were the stochastic surface could be divided into a few different height levels. The valleys in Fig. 1 are of course similar to the hemispherical segments, while the hills can be compared to the non-cratered portion of the simpler approach. A height dependent background field is probably the next step to take in the analytical approach.

The application of the model in practise is demonstrated in Fig. 4. The introduction of surface roughness is a strong effect, and in principle it is possible to obtain surface roughness data from these kind of model-data comparisons. There are, however, several difficulties. The parameters in Table 2 is not taken from a consistent source. The ellipsoidal shape is after all an approximation, and the deviation from the true shape can produce significant effects. The relation between the albedo and the diameter is given from the theory of the HG-system (Bowell et al., 1989), and it is not clear how this relation should be corrected for non-spherical asteroids. This is clearly a problem since the H parameter varies significantly between different investigations for many objects. These and other issues will be discussed in coming papers were the model is applied to a larger data set.

Acknowledgements. I thank Claes-Ingvar Lagerkvist and Karri Muinonen for their comments and general support. On specific topics I thank Per Magnusson for the shape and spin vector of 3 Juno, Thomas Müller for the colour correction of the IRAS data, and Karri for the Gaussian random surfaces. I also thank Dr. L. A. Lebofsky for his review.

Appendix A: Technical details

The details are given to some of the methods used in this paper. Note that by following the authors quoted the notation is conflicting with the notation used above.

A.1. View factors between triangles

The view factors for two finite surfaces can be calculated from Eq. (3) by integrating over their respective surfaces. It is very useful to convert this quadruple integral into two curve integrals by the use of Stokes' theorem twice (Sparrow, 1963):

$$F_{12} = \frac{1}{2\pi s_1} \oint_{\Gamma_1} \oint_{\Gamma_2} \ln\delta \, d\boldsymbol{r}_2 \cdot d\boldsymbol{r}_1$$

where $\boldsymbol{r}_i$ is a point on the curve Γ_i, which in turn outlines the boundary of facet s_i, and $\delta = |\boldsymbol{r}_2 - \boldsymbol{r}_1|$. The orientation of the curves has to be in the positive direction with respect to the normal of each triangle. For a triangle the curve Γ_i is divided into three lines described by

$$\Gamma_{i,k}\colon\ \boldsymbol{r}_{i,k} = \boldsymbol{p}_{i,k} + \boldsymbol{v}_{i,k} t_{i,k} \qquad \text{for } k = 1, 2, 3$$

where the endpoints of the side are given by $t_{i,k} = 0$ and $t_{i,k} = 1$. By this the view factor becomes

$$F_{12} = \frac{1}{2\pi s_1} \sum_{k=1}^{3} \sum_{l=1}^{3} \int_{\Gamma_{1,k}} \int_{\Gamma_{2,l}} \ln\delta \, d\boldsymbol{r}_{2,l} \cdot d\boldsymbol{r}_{1,k}$$

Thus the integration is taken over nine pairs of sides. If the indices k and l are dropped for simplicity, the contribution from one pair (k, l) is

$$\int_{\Gamma_1} \int_{\Gamma_2} \ln\delta \, d\boldsymbol{r}_2 \cdot d\boldsymbol{r}_1 = \boldsymbol{v}_1 \cdot \boldsymbol{v}_2 \int_0^1 \int_0^1 \ln|\boldsymbol{r}_1 - \boldsymbol{r}_2| \, dt_1 \, dt_2$$

If $\boldsymbol{r}_1 - \boldsymbol{r}_2$ is not parallel to $\boldsymbol{v}_1$, the inner integral can be computed analytically by first assuming that

$$\ln\delta = \frac{1}{2}\ln|\boldsymbol{r}_1 - \boldsymbol{r}_2|^2 = \frac{1}{2}\ln(at_1^2 + bt_1 + c)$$

where

$$\begin{aligned} a &= |\boldsymbol{v}_1|^2 \\ b &= -2\boldsymbol{v}_1 \cdot \boldsymbol{v}_2 t_2 + 2(\boldsymbol{p}_1 - \boldsymbol{p}_2) \cdot \boldsymbol{v}_1 \\ c &= |\boldsymbol{v}_2|^2 t_2^2 + 2(\boldsymbol{p}_2 - \boldsymbol{p}_1) \cdot \boldsymbol{v}_2 t_2 + |\boldsymbol{p}_1|^2 + |\boldsymbol{p}_2|^2 - 2\boldsymbol{p}_1 \cdot \boldsymbol{p}_2 \end{aligned}$$

Defining $w = 1/\sqrt{4ac - b^2}$, the integral evaluates to

$$\begin{aligned} \int_0^1 \ln\delta \, dt_1 = &\left(\frac{b}{4a} + \frac{1}{2}\right)\log(a + b + c) - 1 - \frac{b}{4a}\log c \\ &+ w\left(\frac{b^2}{2a} - 2c\right)\big(\arctan wb - \arctan w(2a + b)\big) \end{aligned}$$

If, however, $\boldsymbol{r}_1 - \boldsymbol{r}_2$ is parallel to $\boldsymbol{v}_1$, the degree of the polynomial reduces from 2 to 1. The integral is then evaluated into

$$\int_0^1 \ln\delta\, dt_1 = \left(1+\frac{b}{2a}\right)\log\left|1+\frac{b}{2a}\right| - \frac{b}{2a}\log\left|\frac{b}{2a}\right| + \frac{1}{2}\log a - 1 \quad \text{(A1)}$$

If $\boldsymbol{r}_2$ coincide with one of the endpoints of Γ_1, the integrand $\ln\delta$ approaches a singularity there. The integral still exists, and in Eq. (A1) this handled by $\lim_{x\to 0^+} x\ln x = 0$, where $x \to |b/2a| = 0$, or $x \to |1 + b/2a| = 0$.

There are a few more special cases but for the surfaces considered here, only one of them needs to be discussed further. If the triangles share one side, the singularity will appear on the interval $t_1 \in (0, 1)$, which will require the integral to be divided into two subintervals to avoid the singularity. This procedure leads to

$$\int_0^1\int_0^1 \ln\delta\, dt_1\, dt_2 = \frac{1}{2}\log a + \int_0^1\int_0^1 \ln|t_1 - t_2|\, dt_1\, dt_2 = (\log a - 3)/2$$

In most cases, however, the resulting outer integral over t_2 is evaluated numerically. The reduction of the quadruple integral into a single integral improves the accuracy and computational efforts substantially.

A.2. Generating Gaussian random surfaces

The full details behind the process of generating the surfaces are given by Muinonen & Saarinen (1997). In brief, the height above the mean plane is $z = z(x, y)$, and the roughness is described by a correlation function $C_z(\xi, \eta) = C_z(x_1 - x_2, y_1 - y_2)$. The first step is to consider the 2-dimensional Fourier expansion of the surface:

$$z(x,y) = \sum_{p=-N}^{N}\sum_{q=-N}^{N} Z_{pq}\exp i(pKx + qKy), \quad \text{(A2)}$$

where $N \to \infty$ in the limiting case, and $K = \pi/L$ if $2L$ is the period in the x and y-directions.

Assuming a Gaussian correlation function:

$$C_z(\xi,\eta) = e^{-(\xi^2+\eta^2)/2\ell^2}$$

in which ℓ is the correlation length. The 2-dimensional cosine series coefficients of C_z are then given by,

$$c_{pq} = \frac{\pi\kappa^2}{2}(2-\delta_{0p})(2-\delta_{0q})e^{-\pi^2\kappa^2(p^2+q^2)/2},$$

where $\kappa = \ell/L$, and δ_{ij} is the Kronecker delta.

The real and imaginary parts of the Fourier coefficients Z_{pq} are taken to be independent normal distributed random variables, with zero mean and variances given by

$$\mathrm{Var}\,(\Re\, Z_{pq}) = \frac{1}{8}\,(1 + \delta_{p0} + \delta_{q0} + 5\delta_{p0}\delta_{q0})\, c_{pq}\sigma^2$$

$$\mathrm{Var}\,(\Im\, Z_{pq}) = \frac{1}{8}\,(1 + \delta_{p0} + \delta_{q0} - 3\delta_{p0}\delta_{q0})\, c_{pq}\sigma^2$$

To make the heights real valued, it is furthermore required that $Z_{-p,-q} = Z^*_{p,q}$. This produces a surface $z = z(x, y)$, where z is normal distributed with zero mean and standard deviation σ. The roughness of the surface is described by $\rho = \sigma/\ell$, which is the r.m.s. of the slopes $\partial_x z$ and $\partial_y z$.

Gaussian random surfaces are conveniently generated by the use of the 2-dimensional inverse Fast Fourier Transform (FFT), in Eq. (A2). For a finite surface the correlation length should be taken to be small compared to the period $2L$, i.e. a small κ. This gives $z = z(x, y)$ over a square grid in the xy-plane, with $2N + 1$ points along each side. Since the periodicity of the surface is used, the first row and column of the grid is repeated to complete the period. The resulting side has a length $2L$ and consists of $2(N + 1)$ points. The example surface in Fig. 1 was generated using $L = 0.5$, $\sigma = 0.05$, and $\rho = 1$.

A.3. Orienting the ellipsoid

The techniques for determining spin vectors and shapes of asteroids from visual lightcurves have proven to be quite successful (Magnusson et al., 1989). The low order measure of the shape is often to use the ellipsoid. The shape is described by the axis ratios a/b and b/c, where $a > b > c$. The spin vector is usually assumed to be parallel to the c-axis, and its orientation in space is given by the ecliptic coordinates λ_p and β_p (assuming a right handed system).

One angle is remaining in order to specify the orientation of the ellipsoid at a given rotational phase. This is achieved by (Magnusson, private communication) defining

$$\gamma = 360^\circ\frac{t - t_0}{P_\mathrm{sid}} + \gamma_0 \quad \text{(A3)}$$

where γ_0 is the rotational angle at the time $t = t_0$. At this time the there unit vectors parallel to the three axis of the ellipsoid are given in an ecliptic coordinate system by

$$(\hat{\boldsymbol{a}}_0, \hat{\boldsymbol{b}}_0, \hat{\boldsymbol{c}}_0) = \begin{pmatrix} -\sin\lambda_\mathrm{p} & -\sin\beta_\mathrm{p}\cos\lambda_\mathrm{p} & \cos\beta_\mathrm{p}\cos\lambda_\mathrm{p} \\ \cos\lambda_\mathrm{p} & -\sin\beta_\mathrm{p}\sin\lambda_\mathrm{p} & \cos\beta_\mathrm{p}\sin\lambda_\mathrm{p} \\ 0 & \cos\beta_\mathrm{p} & \sin\beta_\mathrm{p} \end{pmatrix}$$

At a time t these vectors has to be transformed by

$$(\hat{\boldsymbol{a}}, \hat{\boldsymbol{b}}, \hat{\boldsymbol{c}}) = (\hat{\boldsymbol{a}}_0, \hat{\boldsymbol{b}}_0, \hat{\boldsymbol{c}}_0)\cdot\begin{pmatrix} \cos\gamma & -\sin\gamma & 0 \\ \sin\gamma & \cos\gamma & 0 \\ 0 & 0 & 1 \end{pmatrix} \quad \text{(A4)}$$

References

Bowell, E., Hapke, B., Domingue, D., Lumme, K., Peltoniemi, J., and Harris, A. W.: 1989, in R. P. Binzel, T. Gehrels, and M. S. Matthews (eds.), Asteroids II, pp 524–556, The University of Arizona Press

Buhl, D., Welch, W. J., and Rea, D. G.: 1968, J. Geophys. Res. **73(16)**, 5 281

Glassner, A. S. (ed.): 1990, Graphics Gems, Academic Press, Inc.

Hansen, O. L.: 1977, Icarus **31**, 456

Hapke, B.: 1993, Theory of Reflectance and Emittance Spectroscopy, Cambridge University Press

Hapke, B.: 1996a, J. Geophys. Res. **101(E7)**, 16 833

Hapke, B.: 1996b, J. Geophys. Res. **101(E7)**, 16 817
Henderson, B. G. and Jakosky, B. M.: 1994, J. Geophys. Res. **99(E9)**, 19 063
Jämsä, S., Peltoniemi, J. I., and Lumme, K.: 1993, Astron. Astrophys. **271**, 319
Johnson, P. E., Vogler, K. J., and Gardner, J. P.: 1993, J. Geophys. Res. **98(E11)**, 20825
Lagerkvist, C. I., Magnusson, P., Williams, I. P., Buontempo, M. E., Argyle, R. W., and Morrison, L. V.: 1992, Astron. Astrophys. Suppl. Ser. **94**, 43
Lagerros, J. S. V.: 1996a, Astron. Astrophys. **310(3)**, 1 011
Lagerros, J. S. V.: 1996b, Astron. Astrophys. **315(3)**, 625
Lagerros, J. S. V.: 1997, Astron. Astrophys. **325(3)**, 1 226
Lebofsky, L. A. and Spencer, J. R.: 1989, in R. P. Binzel, T. Gehrels, and M. S. Matthews (eds.), Asteroids II, pp 128–147, Arizona University Press
Lebofsky, L. A., Sykes, M. V., Tedesco, E. F., Veeder, G. J., Matson, D. L., Brown, R. H., Gradie, J. C., Feierberg, M. A., and Rudy, R. J.: 1986, Icarus **68**, 239
Magnusson, P., Barucci, M. A., Drummond, J. D., Lumme, K., Ostro, S. J., Surdej, J., Taylor, R. C., and Zappalà, V.: 1989, in R. P. Binzel, T. Gehrels, and M. S. Matthews (eds.), Asteroids II, pp 66–97, The University of Arizona Press
Millis, R. L., Wasserman, L. H., Bowell, E., Franz, O. G., White, N. M., Lockwood, G. W., Nye, R., Bertram, R., Klemola, A., Dunham, E., and Morrison, D.: 1981, Astron. J. **86**, 306
Modest, M. F.: 1993, Radiative Heat Transfer, McGraw-Hill Publishing Company, New York, NY
Muinonen, K. and Saarinen, K.: 1997, JQSRT, In preparation
Müller, T.: 1997, Ph.D. thesis, Ruprecht-Karls-Universität, Heidelberg
Saari, J. M. and Shorthill, R. W.: 1972, The Moon **5**, 161
Saari, J. M., Shorthill, R. W., and Winter, D. F.: 1972, The Moon **5**, 179
Sparrow, E. M.: 1963, ASME J. Heat Transfer **85**, 81
Spencer, J. R.: 1990, Icarus **83**, 27
Tedesco, E. F., Veeder, G. J., Fowler, J. W., and Chillemi, J. R.: 1992, IRAS Minor Planet Survey, Jet Propulsion Laboratory
Vogler, K. J., Johnson, P. E., and Shorthill, R. W.: 1991, Icarus **92**, 80
Winter, D. F. and Krupp, J. A.: 1971, The Moon **2**, 279